

Alma Mater Studiorum Università di Bologna  
Archivio istituzionale della ricerca

Interfaces within biphasic nanoparticles give a boost to magnesium-based hydrogen storage

This is the final peer-reviewed author's accepted manuscript (postprint) of the following publication:

*Published Version:*

Patelli N., Migliori A., Morandi V., Pasquini L. (2020). Interfaces within biphasic nanoparticles give a boost to magnesium-based hydrogen storage. NANO ENERGY, 72, 1-10 [10.1016/j.nanoen.2020.104654].

*Availability:*

This version is available at: <https://hdl.handle.net/11585/752696> since: 2020-03-23

*Published:*

DOI: <http://doi.org/10.1016/j.nanoen.2020.104654>

*Terms of use:*

Some rights reserved. The terms and conditions for the reuse of this version of the manuscript are specified in the publishing policy. For all terms of use and more information see the publisher's website.

This item was downloaded from IRIS Università di Bologna (<https://cris.unibo.it/>).  
When citing, please refer to the published version.

(Article begins on next page)

## Interfaces within biphasic nanoparticles give a boost to Magnesium-based hydrogen storage

Nicola Patelli<sup>a</sup>, Andrea Migliori<sup>b</sup>, Vittorio Morandi<sup>b</sup>, Luca Pasquini<sup>a\*</sup>

*a.* Department of Physics and Astronomy, University of Bologna, viale Berti-Pichat 6/2, 40127 Bologna, Italy

*b.* Unit of Bologna, Institute for Microelectronics and Microsystems, National Research Council, via Gobetti 101, 40129 Bologna, Italy

\* *Corresponding author:* Prof. Luca Pasquini, [luca.pasquini@unibo.it](mailto:luca.pasquini@unibo.it)

### Abstract:

The use of Mg as hydrogen storage material is hampered by slow sorption kinetics and high thermodynamic stability. This work reports on biphasic Mg-Ti-H nanoparticles that outperform known Mg-based materials in both respects. By exploiting gas-phase condensation of Mg and Ti vapors under He/H<sub>2</sub> atmosphere, biphasic nanoparticles are grown, in which the bulk-immiscible MgH<sub>2</sub> and TiH<sub>2</sub> phases are mixed at the nanoscale. TiH<sub>2</sub> conveys catalytic activity for H<sub>2</sub> dissociation/recombination and accelerated hydrogen diffusion, while MgH<sub>2</sub> provides reversible hydrogen storage. At the remarkably low temperature of 150 °C, hydrogen absorption and desorption are completed in less than 100 s and 1000 s, respectively. Moreover, the equilibrium pressure for hydrogen sorption exhibits a composition-dependent upward shift compared to bulk Mg, resulting in a pressure increase by a factor of about 4.5 in the Ti-richest samples at 100 °C. The enthalpy and entropy of the metal-hydride transformation are both lower in magnitude with respect to the bulk values, suggesting opposite contributions to the free energy change. The results are analyzed by an interface-induced hydride destabilization model, determining an interfacial free energy difference  $\Delta\gamma = (0.38 \pm 0.04) \text{ Jm}^{-2}$  between hydride and metal phases at T=100 °C. These unique composite nanoparticles significantly extend the temperature/pressure window of hydrogen storage applications using Mg-based materials compatible with up-scaling.

### Keywords

hydrogen storage, magnesium, nanoparticles, interfaces, gas phase condensation

## 1. Introduction

Hydrogen (H) represents the ultimate energy carrier due to its lightness, high abundance and potentially zero environmental impact. Its low mass results in unparalleled gravimetric energy density ( $142 \text{ MJ kg}^{-1}$ ), about 3 times higher than liquid hydrocarbons. Hydrogen can be produced from water using renewable energy, either by integrating alkaline electrolyzers [1] with photovoltaic power generation or by photoelectrochemical water splitting exploiting sunlight [2]. In combination with oxygen in a fuel cell, it produces electricity and yields only clean water vapor as exhaust product [3,4], therefore its use in the transportation sector would significantly abate atmospheric pollution. This scheme builds up a carbon-neutral energy cycle, also offering a viable solution to the problem of storing energy from intermittent sources such as sunlight and wind.

The principal disadvantage of hydrogen is the very low temperature of its critical point (33.2 K), which makes it quite impractical to handle liquid  $\text{H}_2$  in everyday's life [5]. Due to the low volumetric density of the gas, there is a need to develop compact hydrogen storage media in order to manage efficiently hydrogen production and use. An attractive solution in this respect is provided by solid-state hydrogen storage in hydrides [6], since it can achieve a volumetric density above  $100 \text{ kg H}_2 \text{ m}^{-3}$ , i.e. well above liquid  $\text{H}_2$  ( $70 \text{ kg H}_2 \text{ m}^{-3}$ ) and  $\sim 3$  times higher than pressurized tanks ( $<40 \text{ kg H}_2 \text{ m}^{-3}$  at 70 MPa), moreover allowing for operation under safe pressure conditions. Among the numerous materials investigated to this purpose, magnesium hydride ( $\text{MgH}_2$ ) remains a prominent candidate by virtue of high gravimetric (7.6 wt%  $\text{H}_2$ ) and volumetric ( $109 \text{ kg H}_2 \text{ m}^{-3}$ ) storage capacities, high abundance (2% of Earth surface composition and almost unlimited in sea water), non-toxicity, and relatively safe operation [7,8]. However, the exploitation of Mg as H-storage medium has been hampered by its slow absorption and desorption kinetics and high thermodynamic stability, both usually requiring high operating temperatures of about  $300^\circ\text{C}$ . In this work, we present the new concept of biphasic Mg-Ti-H nanoparticles (NPs) that outperform existing Mg-based materials both from the kinetic and thermodynamic point of view.

The fundamental sources of kinetics and thermodynamics limitations in Mg/ $\text{MgH}_2$  are of different nature [9,10]. In fact, sluggish kinetics relate to both surface and bulk properties. Theoretical calculations of Mg surfaces show very low rates of both  $\text{H}_2$  dissociation and recombination, which are required steps for hydrogen absorption and desorption, respectively [11]. The rapid formation of  $\text{MgO}$  or  $\text{Mg(OH)}_2$  passivating surface layers, that takes place even under clean atmosphere, aggravates the situation [12]. As for bulk properties, the formation of a  $\text{MgH}_2$  outer layer during hydriding, coupled with the slow diffusivity of hydrogen through  $\text{MgH}_2$ , results in a so-called blocking effect that strongly slows down H-absorption kinetics [13]. On the other hand, thermodynamics reflects the strength of the Mg-H bond and dictates the equilibrium pressure / temperature conditions for hydrogen uptake and release. With a strongly negative enthalpy of hydride formation  $\Delta H \approx -74 \text{ kJ/mol H}_2$ , and a formation entropy

$\Delta S \approx -133 \text{ J/K}\cdot\text{mol H}_2$  [14], H-desorption from  $\text{MgH}_2$  at atmospheric pressure can only take place above  $T = 282 \text{ }^\circ\text{C}$

It is important to remark that kinetics and thermodynamics of hydrogen sorption exhibit no straightforward relation. For instance, in  $\text{TiH}_2$  the stronger Ti-H bond results in an even less favorable thermodynamics compared to  $\text{MgH}_2$ , with a formation enthalpy  $\Delta H \approx -130 \text{ kJ/mol H}_2$  [15]. However, H-sorption kinetics are faster, because i)  $\text{H}_2$  dissociation and recombination at the surface is favored by the availability of s-type orbitals around the Fermi level [16] and ii) atomic hydrogen diffuses rapidly in  $\text{TiH}_2$ , e.g. the characteristic time for a diffusion length of 13 nm is only 22 s [17]. It is therefore by no means obvious how to steer both kinetics and thermodynamics in the right direction at the same time.

In the case of  $\text{Mg/MgH}_2$ , H-sorption can be significantly enhanced by grain refinement coupled with the addition of suitable additives such as transition metal oxides [18,19] and hydrides [20]. The most popular synthesis route has been mechanochemistry through ball milling that yields  $\text{MgH}_2$  particles of about 2-5  $\mu\text{m}$  in diameter with a dispersion of smaller nanoparticles (10-20 nm) of the additive phases. Among the best performances reported within the vast literature on the subject, we cite  $\text{MgH}_2\text{-TiH}_2$  ball-milled nanocomposites, showing a  $\text{H}_2$  desorption rate of about 3.2 wt%/min at  $T = 300 \text{ }^\circ\text{C}$  [17] that strongly decreases down to 0.10 wt%/min at  $150 \text{ }^\circ\text{C}$  even under high vacuum conditions [21]. Another benchmark example is that of ball-milled  $\text{MgH}_2\text{-Nb}_2\text{O}_5$  that exhibits a similar desorption rate (into vacuum) of about 4 wt%/min at  $T = 300 \text{ }^\circ\text{C}$  and 0.6 wt%/min at  $250 \text{ }^\circ\text{C}$  [22].

However, the thermodynamics of these microstructures is essentially the same as bulk  $\text{Mg}$ , because the  $\text{MgH}_2$  particle size is too large and the interface/surface area too small [23–25]. Until today, significant changes in the thermodynamics of hydrogen desorption by  $\text{MgH}_2$  have been reported only in ultra-thin films ( $< 10 \text{ nm}$ ) generally embedded within  $\text{TiH}_2$  and have been attributed to the interface free energy change upon H-sorption [26,27]. The key to observe a measurable effect is the high interface area per molar volume of the material. While ultra-thin films are extremely useful model systems to study such effects and may find applications in sensors [28], they fail to comply with the possibility of upscaling, which is needed for a hydrogen storage application. Moreover, all experiments in  $\text{Mg}$ -based thin films employed a Pd capping layer to protect the samples and promote  $\text{H}_2$  dissociation/recombination.

Herein, we provide evidence of simultaneous improvement in kinetics and thermodynamics for  $\text{Mg-Ti-H}$  composite NPs, the length scale of which is two orders of magnitude smaller than for conventional ball-milled powders. We obtain an ultra-fine mixing of  $\text{MgH}_2$  and  $\text{TiH}_2$  phases within single nanoparticles grown by gas-phase condensation of  $\text{Mg}$  and  $\text{Ti}$  vapors under  $\text{He/H}_2$  atmosphere. This is noteworthy because  $\text{Mg}$  and  $\text{Ti}$  are bulk-immiscible both as metals and as hydrides. The unique nanostructure of these samples combines the high interface area featured by ultra-thin films with the three-dimensional scalable morphology of powders. Therefore, by a suitable up scaling of the NPs preparation equipment, it would be possible to conceive a high throughput production of a hydrogen storage medium unaffected by the severe volumetric and

gravimetric penalty of supported thin films. The Mg-Ti-H composite NPs feature full H<sub>2</sub> desorption at temperatures as low as 150 °C, at a rate between 0.1 and 0.2 wt%/min against a pressure of about 100 Pa. Moreover, the equilibrium H<sub>2</sub> pressure increases by a factor of up to  $\approx 4.5$  at  $T = 100$  °C compared to bulk-like MgH<sub>2</sub>, being similar to that observed in 2 nm thin films. Remarkably, these results are achieved without using Pd as H<sub>2</sub> dissociation/recombination catalyst and with a maximum reversible H-storage capacity that approaches 5 wt% for the best Ti/Mg atomic ratio.

## 2. Material and methods

### 2.1 Preparation of nanoparticles

Mg-Ti-H nanoparticles (NPs) were grown by Gas Phase Condensation (GPC) of mixed Mg-Ti vapors under an equimolar H<sub>2</sub>/He gas atmosphere at the total pressure  $p \sim 260$  Pa. The growth process was carried out in an ultra-high vacuum (UHV) stainless-steel chamber previously evacuated to the base pressure  $\approx 2 \times 10^{-5}$  Pa. The precursor materials, Mg ingots (*Alpha Aesar* 99.95% purity) and Ti powders (*Alpha Aesar* 99.9% purity, 150 mesh), were evaporated inside two Joule-heated tungsten boats positioned few centimeters apart in order to favor the vapor mixing. The metal vapors lose kinetic energy through collisions with the surrounding gas atmosphere and attain a supersaturation state that leads to homogeneous condensation of NPs. The evaporation rates of Mg and Ti were monitored by means of a quartz crystal microbalance and tuned by controlling the heating currents, in order to prepare samples with different Ti content. From now on, the samples will be labelled as Mg- $X_{Ti}$ -Ti-H, where the average Ti atomic percentage  $X_{Ti}$  is defined as  $X_{Ti} \equiv 100 \cdot Ti/(Ti+Mg)$ .

He (99.9996%) and H<sub>2</sub> (99.995%) were continuously fed into the chamber at a constant flow rate of 5 nml/min by means of two mass flow controllers, while a rotary pump connected to the chamber via a metering valve counteracted the inlet flow, dynamically maintaining a constant gas pressure. The NPs aerosol was collected onto the surface of a stainless-steel rotating cylinder internally cooled by liquid N<sub>2</sub>. After the evaporation, the NPs were scraped off the cylinder under high vacuum, collected into a stainless-steel cup and transferred into a secondary UHV chamber for *in situ* characterization of hydrogen sorption properties. **Figure S1** of the Supporting Information displays a detailed mechanical drawing of the NPs preparation set-up.

### 2.2 In-situ hydrogen sorption measurements

The secondary chamber had a total volume of 5144 cm<sup>3</sup> calibrated by means of a reference volume using a pressure sensor. The NPs sample, with a typical mass of about 50 mg, was held inside a glass vial connected to a sub-section with a smaller volume of 1888 cm<sup>3</sup> that could be isolated via a gate valve to achieve a higher sensitivity to hydrogen uptake and release. A small tubular oven with a resistive wire heater, variable power supply and feedback thermocouple in contact with the sample holder allowed for the realization of isothermal conditions in the range from 100 to 150 °C. The thermocouple was calibrated by comparison with a semiconductor

thermistor. The temperature accuracy was estimated as  $\pm 0.5$  °C and the temperature stability was also in that range, yielding an overall temperature uncertainty of  $\pm 1$  °C.

The hydrogen pressure  $p(\text{H}_2)$  in the  $1 - 2 \cdot 10^4$  Pa range was measured using a Varian ceramic capacitance diaphragm gauge (CDG) pressure sensor. At low pressure, the sensor output was amplified 100 times to achieve the necessary sensitivity; the sensor signal was digitized by a 16-bit analog-to-digital converter.

As a first treatment, the as-prepared NPs were soaked in hydrogen ( $p(\text{H}_2) = 20$  kPa) at room temperature and then heated at 150 °C for 1 hour to induce the complete hydride formation.

One set of samples with  $X_{\text{Ti}} = 7, 35, 63$  at.% was employed to study pressure-dependent hydrogen absorption and desorption kinetics at 150 °C, starting with a desorption from the hydride state. The kinetics were determined by recording the pressure change  $\Delta p(t)$  at 150 °C until the pressure remained essentially constant. The asymptotic pressure change was of the order of 100 Pa, depending on the Ti content and on the sample mass. In the case of absorption, this was much smaller than the initial pressure and therefore the kinetics were quasi-isobaric, thus maintaining nearly constant the driving force of the transformation. Differently, for desorption kinetics the initial pressure was quite low, typically only 10 Pa, as requested in order to start well below the desorption plateau pressure. Therefore, the conditions could not be maintained nearly isobaric. To overcome this limitation, desorption kinetics were also determined under high vacuum conditions  $p(\text{H}_2) < 10^{-2}$  Pa by measuring the ion current associated with the  $m/q = 2$  mass-to-charge ratio with a quadrupole mass spectrometer (model *Pfeiffer QMS-200*).

After ten cycles of desorption/absorption kinetics, one full desorption/absorption pressure-composition-isotherm (PCI) was recorded at 150 °C. The PCIs were determined by the manometric method, i.e. by monitoring pressure changes  $\Delta p(t)$  after stepwise increments (absorption branch) or decrements (desorption branch) of the hydrogen pressure. The measurements were carried out under quasi-equilibrium conditions, with a waiting time of 1000 s between two subsequent pressure steps. Due to the lower limit of the pressure sensor, it was not possible to collect accurate equilibrium pressure data below 1 Pa. The measured  $\Delta p(1000 \text{ s})$  values were converted into moles of absorbed or desorbed hydrogen and finally into a hydrogen-to-metal mass ratio (H/M in wt%) by knowing the calibrated volume and the sample mass. High vacuum coupled with mass spectrometry analysis was also used to quantify the amount of desorbed hydrogen in the low-pressure final part of the PCI desorption branch.

A second set of samples with  $X_{\text{Ti}} = 14, 22, 46, 63$  at.% was employed to study the temperature dependence of the plateau pressures and to construct the van 't Hoff plots, from which thermodynamic data were obtained. The plateau pressures for absorption and desorption were determined from PCIs steps carried out at  $T = 150, 137, 125, 112$ , and 100 °C. The measurement sequence was designed in order to limit coarsening phenomena during the measurements. In fact, even if Ti helps as a nanostructure refiner, the formation of larger NPs

and the segregation of Ti was spotted by electron microscopy analysis of the NPs subjected to several H-sorption cycles. Moreover, the relative MgO amount can also increase upon cycling, which could deteriorate the H-sorption kinetics and affect the determination of equilibrium. This issue may be solved in the future by filtering oxygen and moisture impurities and/or by optimizing the amount of material relative to the reaction chamber. Here, we adopted an experimental strategy that minimizes contamination and coarsening while conveying the relevant data to assess the thermodynamic equilibrium conditions. Full details about the experimental sequence are provided in the Supporting Information.

### 2.3 Structural, chemical and morphological characterization

Prior to their extraction from the UHV system, the NPs were subjected to a final H-absorption at  $T = 150\text{ }^{\circ}\text{C}$  and  $p(\text{H}_2) = 15 - 20\text{ kPa}$ , after which the glass vial containing the sample was cooled to room temperature and filled with pure Argon at atmospheric pressure. The sample vial was finally sealed under Ar for further analyses.

The previously defined average Ti content  $X_{\text{Ti}}$  in each sample was determined employing a *Leica Cambridge Stereoscan 360* scanning electron microscope (SEM) equipped with an *Oxford Instruments* X-ray detector for energy dispersive X-ray microanalysis.

Microstructural and nanoscale compositional analyses were performed by using a *Philips TECNAI F20 ST* transmission electron microscope (TEM) operating at 200 kV. The instrument is equipped with dispersion micro-analysis of energy (EDS) and scanning transmission (STEM) accessory. The TEM images were taken in the phase contrast mode. STEM pictures were recorded using a High Angle Annular Dark Field (HAADF) detector. Selected Area electron Diffraction (SAD) patterns were processed using the PASAD plugin developed for the *Digital Micrograph* software to determine the azimuthal integration profiles[29]. For (S)TEM observations, a sealed vial containing the NPs was filled with isopropyl alcohol using a syringe that perforated the plastic cap. The obtained suspension was sonicated, and few drops of the suspension were casted on a copper grid coated with an amorphous carbon film.

The lattice parameters and the crystallite size of the phases constituting the samples were determined by X-ray diffraction (XRD) using a *PANalytical X'celerator* diffractometer employing  $\text{Cu K}\alpha$  radiation. The XRD profiles were analyzed using the MAUD full-profile refinement software [30].

## 3. Results and Discussion

### 3.1 Structural Characterization

The typical morphology of Mg-Ti-H NPs prepared by GPC and subjected to a single hydrogen loading at  $150\text{ }^{\circ}\text{C}$  is illustrated by **Figure 1 (a,c)**, showing the two samples Mg-14Ti-H and Mg-63Ti-H. The average size of the primary NPs decreases from  $d_{\text{NP}} \approx 26\text{ nm}$  for low  $X_{\text{Ti}}=7\text{ at.}\%$  to  $d_{\text{NP}} \approx 10\text{ nm}$  for high  $X_{\text{Ti}}$ , as reported in Table S1. The NPs exhibit significant aggregation, as commonly observed in GPC due to partial sintering in proximity of the hot vapor source [31,32].



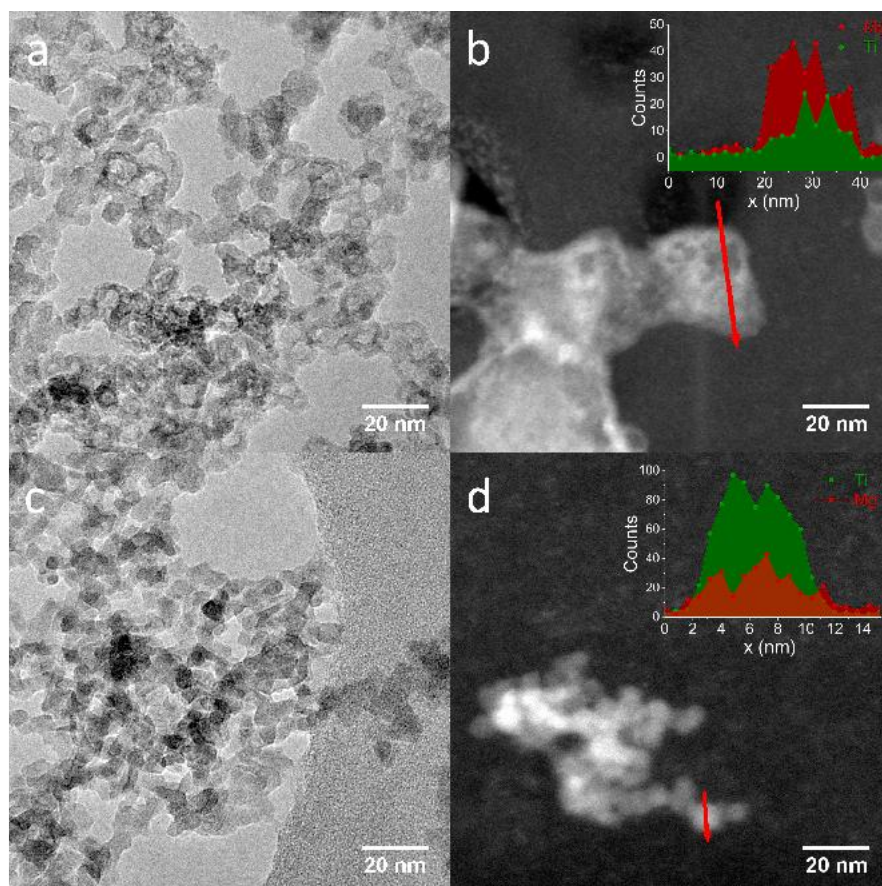


**Figure 1.** Bright field TEM images (left column: **a,c**) and HAADF-STEM images with EDS line scans (right column: **b,d**) of samples Mg-14Ti-H (top row: **a,b**) and Mg-63Ti-H (bottom row: **c,d**). **a,c** are NPs subjected to a single hydrogen loading at 150 °C, which are representative of the primary NPs. **b,d** are cycled NPs used for the construction of van 't Hoff plots. The insets in **b,d** represent the K-line counts of Mg and Ti along the line scans indicated by the red arrows.

The peculiarity of these samples is that each NP contains both Mg and Ti, the two elements being finely distributed at the nanoscale despite their mutual immiscibility in the bulk. This feature is highlighted in **Figure 1 (b,d)** by the STEM-EDS line scans taken across individual NPs after H-sorption cycling, similar results being obtained on all NPs for every composition. We notice that the K-line X-rays of both Mg and Ti are detected at each point inside the NPs. The fluctuations of the Mg/Ti ratio along the scans sometimes exceed the statistical uncertainty, indicating that the two elements do not form a homogeneous solid solution and that segregation into Mg-rich and Ti-rich domains takes place. This view is consistent with the picture provided by XRD, as discussed in the following.



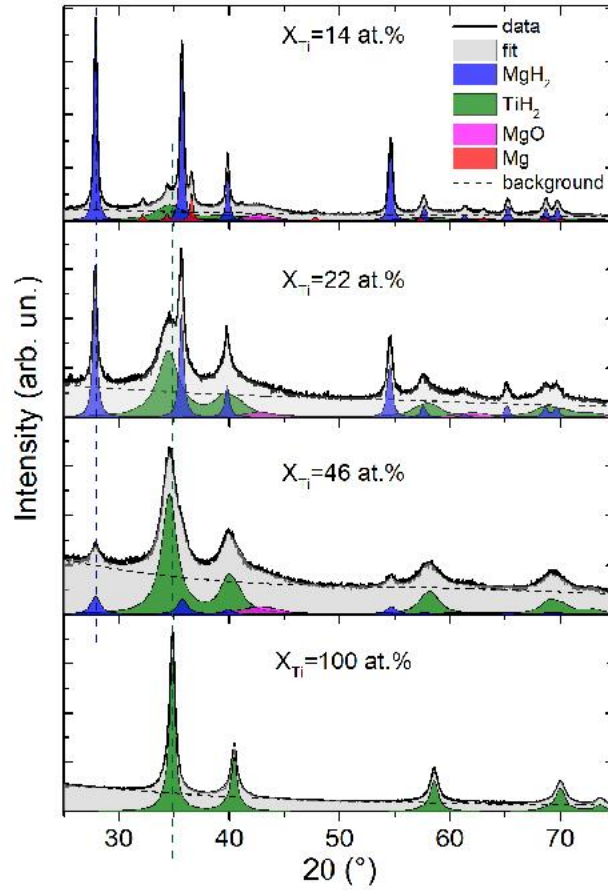


**Figure 2.** X-ray diffraction profiles (black solid lines) as a function of the Ti content  $X_{\text{Ti}}$ . The grey area represents the best fit obtained with the refinement program MAUD; the coloured peaks highlight the corresponding contributions from the various crystalline phases, while the black dashed curve denotes the instrumental background. The vertical dashed lines mark the angular position of the  $\text{MgH}_2$  (110) and  $\epsilon\text{-TiH}_2$  (101) Bragg reflections, the latter shifting to lower angles with increasing Mg content.

The XRD profiles in **Figure 2** show that the crystalline phases after H-absorption are tetragonal  $\text{MgH}_2$  (space group  $P42/mnm$ ),  $\text{TiH}_2$  and  $\text{MgO}$ . In addition, a small amount of metallic Mg is detected in the samples with lower  $X_{\text{Ti}}$  of 7 and 14 at.%, indicating that H-absorption is not complete within the time-temperature window of the measurements described in the next section. The Bragg reflections associated with  $\text{TiH}_2$  are rather broad, pointing to a small crystallite size that ranges from about 3.5 nm at low  $X_{\text{Ti}}$  to about 7 nm at high  $X_{\text{Ti}}$  (see **Table S1** in the Supporting Information). This makes it difficult to distinguish between the fluorite-type cubic  $\text{TiH}_2$  (space group  $Fm\bar{3}m$ ) and its distorted tetragonal variant  $\epsilon\text{-TiH}_2$  (space group  $I4/mmm$ ). Goodness of fit indicators are in favor of the tetragonal phase, in agreement with our previous reports [33,34]. With increasing Mg content, the Bragg reflections of  $\epsilon\text{-TiH}_2$  shift toward lower angles, indicating an expansion of the  $\epsilon\text{-TiH}_2$  unit cell volume by 2 – 4 % (see lattice parameters in **Table S1**) that may arise from solubility of Mg, whose atomic radius is larger than Ti. The observed expansion corresponds to a 6 – 10 at.% Mg solubility within  $\epsilon\text{-TiH}_2$ .

domains [34]. Conversely, for  $\text{MgH}_2$  the Bragg angles and the derived lattice parameters are not affected by  $X_{\text{Ti}}$ , indicating that the solubility of Ti in  $\text{MgH}_2$  is certainly below 1 at.% [33]. The crystallite sizes of both hydride phases strongly correlate with their relative amount. In particular, the decreasing content of one phase comes along with the increasing crystallite size of the other (**Table S1**), showing that each hydride acts as a grain refiner and/or coarsening inhibitor for the other, a phenomenon already reported for hydride-based composites [17,20]. This effect already takes place while NPs nucleate and grow in the gas phase [33,35] and becomes more important during H-sorption cycles. A clear example of cycling-induced morphological evolution for  $X_{\text{Ti}} = 14$  at.% is conveyed by **Figure 1b**, showing cycled NPs that are significantly larger than the corresponding primary NPs of **Figure 1a**. In samples Mg-7Ti-H and Mg-14Ti-H, the average NPs diameter observed by TEM after cycling is  $d_{\text{NP}} \approx 40$  nm, while in Mg-22Ti-H  $d_{\text{NP}} \approx 30$  nm. These values are similar to the  $\text{MgH}_2$  crystallite size given by XRD, consistently with the observation that the NPs are mostly single-crystalline. For the other samples with higher Ti contents, we did not detect a significant evolution of the NPs size upon cycling. The increased NPs size likely slows down H-sorption kinetics, which may explain the presence of residual metallic Mg for samples Mg-7Ti-H and Mg-14Ti-H. As a possible coarsening mechanism, we propose that sintering occurs between metallic Mg NPs after H-desorption, on account of the low melting point of Mg. In the subsequent H-absorption, the  $\text{MgH}_2$  phase nucleated at the grain boundary between sintered NPs may grow into a larger crystallite. However, unravelling the atomistic coarsening mechanisms would require dedicated experiments, possibly including *in situ* observations, which are beyond the scope of the present work.

In summary, STEM-EDS shows that Mg and Ti are present inside each NP with a composition that fluctuates around the overall average value for each sample, while XRD shows that the main phases are  $\text{MgH}_2$  and  $\text{TiH}_2$ , with little or no mutual solubility. The combination of these results therefore proves that  $\text{MgH}_2$  and  $\text{TiH}_2$  coexist at the single NPs level. Unfortunately, it is not possible to record high resolution TEM images of  $\text{MgH}_2/\text{TiH}_2$  interfaces because  $\text{MgH}_2$  readily decomposes under the electron beam [36], yielding metallic Mg and MgO. Such a decomposition is proved by the SAD pattern with azimuthal integration displayed in **Figure 3a** for the sample Mg-14Ti-H. In comparison with the XRD pattern in **Figure 2**, we notice a strong increase in the diffracted intensity by Mg and MgO at the expenses of  $\text{MgH}_2$ . After prolonged e-beam exposure, we do not observe any  $\text{MgH}_2$  diffraction spots, hinting at its full decomposition. At low  $X_{\text{Ti}}$  it is also difficult to detect the electron diffraction of  $\text{TiH}_2$  because the corresponding rings partially overlap with those of Mg and are quite faint due to the small crystallite size. At high Ti contents, only  $\text{TiH}_2$  and MgO are detected by electron diffraction following  $\text{MgH}_2$  decomposition under the electron beam, as shown in **Figure 3b** for sample Mg-46Ti-H. The absence of metallic Mg may be due to the smaller NPs size that facilitates full oxidation by residual gaseous impurities in the TEM column.

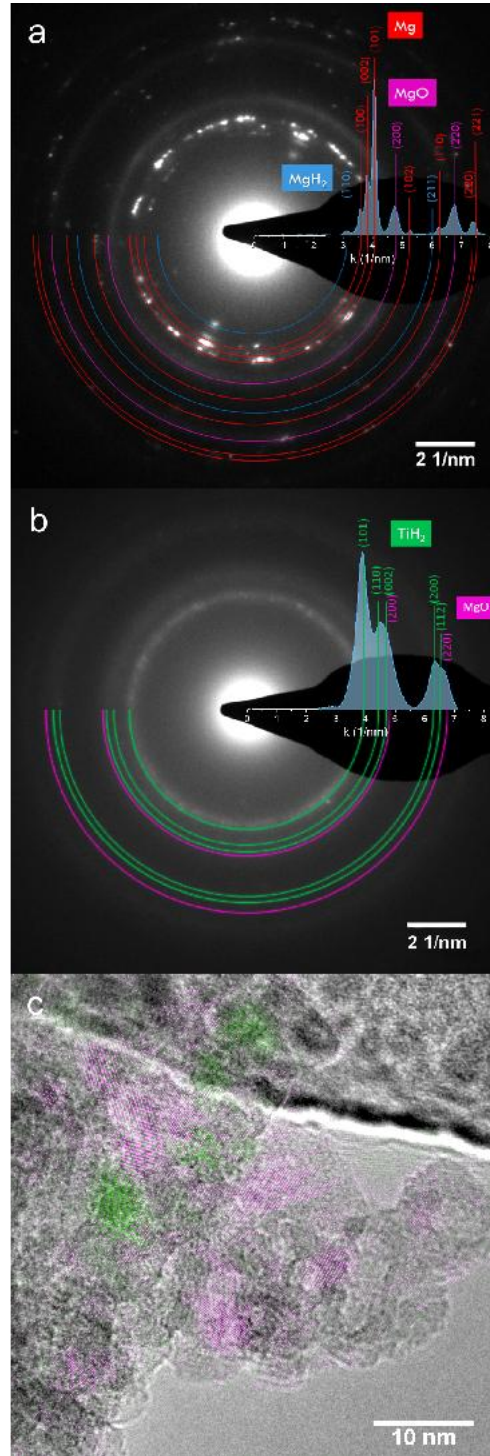


**Figure 3. a,b:** SAD patterns of samples Mg-14Ti-H (a) and Mg-46Ti-H (b). The overlaid blue plot is obtained by azimuthal integration as a function of the reciprocal vector  $k$ . The diffraction rings of the identified phases are highlighted using different colors. **c:** HR-TEM image of the sample in **b** with  $X_{\text{Ti}} = 46$  at.%. The MgO {200} and  $\epsilon$ -TiH<sub>2</sub> {101} families of lattice planes are highlighted in magenta and green, respectively.

In this sort of *post mortem* scenario, one can figure out the original spatial distribution of  $\text{TiH}_2$  and  $\text{MgH}_2$  phases through HR-TEM images that highlight the lattice spacing of  $\text{TiH}_2$  and  $\text{MgO}$ , as shown in **Figure 3c**. Here,  $\text{TiH}_2$  crystallites smaller than 10 nm are here seen in close proximity to  $\text{MgO}$  crystallites, a clear indication that many  $\text{MgH}_2/\text{TiH}_2$  interfaces were present in the samples before decomposition. These interfaces are the subject of the subsequent discussion centered on improved hydrogen thermodynamics and kinetics of Mg-Ti-H NPs.

### 3.2 Hydrogen Sorption Thermodynamics

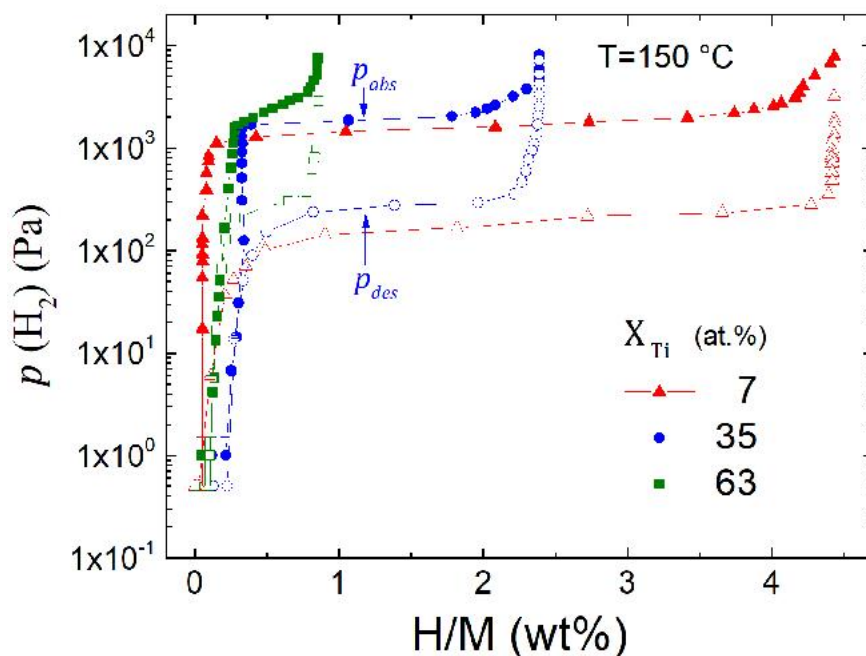


**Figure 4.** PCIs recorded at 150 °C on three samples with  $X_{\text{Ti}} = 7$ , 35, and 63 at.%. Absorption and desorption data are represented using full and open symbols, respectively. The mid-plateau pressures for hydrogen absorption ( $p_{\text{abs}}$ ) and desorption ( $p_{\text{des}}$ ) are marked by solid arrows for sample Mg-35Ti-H.

**Figure 4** displays the PCIs recorded at 150 °C on three samples with  $X_{\text{Ti}} = 7$ , 35, and 63 at.%, covering the widest compositional range available in the present work. The same data are plotted on a normalized horizontal scale from 0 to 1 in **Figure S2** of the Supporting Information. Actually, these PCIs were recorded after a set of ten desorption/absorption kinetics, presented later on in Section 3.3. We notice that it is not possible to compare directly these data with bulk Mg because its kinetics are so sluggish that no measurable hydrogen sorption takes place at this temperature under close to equilibrium conditions. The inspection of the figures highlights several distinct features, discussed here below, which reveal a composition-dependent thermodynamics in Mg-Ti-H NPs.

- The gravimetric reversible H-storage capacity decreases with increasing Ti content. This is because the main contribution to reversible H-storage arises from the  $\text{Mg} + \text{H}_2 \leftrightarrow \text{MgH}_2$  reaction. In fact,  $\text{TiH}_2$  does not decompose under the pressure/temperature conditions of

our experiments. There is, however, a reversible capacity likely associated with  $\text{Mg}_{4-n}\text{Ti}_n$  clusters, which release hydrogen at low pressure but still within the range of the experiments, as discussed next.

- Besides the main absorption and desorption plateaus shown by all samples in the H-rich part of the PCIs, the two Ti-rich samples exhibit reversible H-sorption at much lower pressure. The sensor range and the pressure control system of the *in situ* setup did not allow the accurate determination of low equilibrium pressures, and we can only state that the equilibrium pressure of the low-pressure H-sorption process is lower than the experimental limit, i.e.  $\leq 1$  Pa. The relative importance of the low-pressure H-sorption on the overall reversible H-capacity increases with Ti content as shown by **Figure S2**. Previous studies on  $\text{Mg}_{1-x}\text{Ti}_x\text{H}_y$  thin films showed that several low-pressure plateaus are associated with H-sorption by  $\text{Mg}_{4-n}\text{Ti}_n$  clusters in a metastable solid solution [37]. We therefore suggest that the low-pressure H-sorption originates with the solution of Mg in  $\text{TiH}_2$ , as indicated by XRD analysis. In the following, the discussion of H-sorption thermodynamics will focus on the main plateau at higher pressure associated with the  $\text{Mg} + \text{H}_2 \leftrightarrow \text{MgH}_2$  reaction.
- Figure 4 and Figure S2 show that the mid-plateau pressures for both desorption ( $p_{des}$ ) and absorption ( $p_{abs}$ ) are higher in the Ti-rich samples compared to Mg-7Ti-H. This result points to an upward shift of the equilibrium pressure, i.e. a destabilization of the hydride, with increasing Ti content.

The upward shift of the desorption plateau is noteworthy, because it is a signature of destabilization that is not always present in Mg-based nanostructures. For instance, in elastically clamped Mg-Pd alloy thin films,  $p_{abs}$  was clearly composition-dependent and could be shifted upward by exploiting elastic constraints, while  $p_{des}$  was not [38]. Also in Mg-Ti-Pd layered nanodots it was observed that the  $p_{abs}$  increased with decreasing nanodots size, while  $p_{des}$  remained essentially unchanged [39]. A thickness-dependent upward shift of both  $p_{abs}$  and  $p_{des}$  was reported for quasi-free  $\text{MgH}_2$  thin films sandwiched within  $\text{TiH}_2$  layers [26], as well as for  $\text{MgH}_2$  clusters embedded in a  $\text{TiH}_2$  film [27].

In order to assess the temperature and composition dependence of equilibrium pressures, we have proceeded to determine  $p_{abs}$  and  $p_{des}$  on another set of four samples with  $X_{\text{Ti}} = 14, 22, 46$  and  $63$  at.%. These samples were subjected to a single desorption/absorption cycle at  $150^\circ\text{C}$ , during which kinetics were measured, prior to carrying out PCI steps at five temperatures in the range  $100 - 150^\circ\text{C}$  ( $373 - 423$  K), as detailed in the Supporting Information. The equilibrium pressure was calculated as:

$$p_{eq} = (p_{abs} \cdot p_{des})^{1/2} \quad (1)$$

The results are summarized in **Figure 5**, where the colored dashed lines represent best fits according to the van 't Hoff equation for the different compositions. It is interesting to compare these data with those measured at  $90^\circ\text{C}$  for unclamped Mg films of 2 and 50 nm [26], also

displayed in **Figure 5**. The 2 nm Mg film appears to almost lie on the line of Mg-63Ti-H NPs, while the thicker 50 nm film has a much lower  $p_{eq}$ , which lies on the black dash-dotted van 't Hoff line in **Figure 5**, calculated using the thermodynamic parameters of bulk Mg  $\Delta H_{bulk}^0 = -74.1$  kJ/molH<sub>2</sub> and  $\Delta S_{bulk}^0 = -133.4$  J/K · molH<sub>2</sub> [14]. We remark again that no experimental values are available for bulk Mg in this temperature range, and that the above parameters were obtained from equilibrium data collected around 300 °C. Nevertheless, the fact that the calculated dash-dotted line crosses the experimental  $p_{eq}$  value of a relatively thick, unclamped Mg film supports the validity of this extrapolation. The equilibrium value previously measured on similar Mg-6Ti-H NPs at 100 °C is also reported [33]. The important message of **Figure 5** is that  $p_{eq}$  lies clearly above the line of bulk Mg for all Mg-Ti-H NPs and tends to shift upward with increasing Ti content, although both data and fit for  $X_{Ti} = 14$  and 22 at.% are nearly superposed and indistinguishable within the experimental uncertainties. These considerations hold also for the separate  $p_{abs}$  and  $p_{des}$  data reported in **Figures S3** and **S4**.

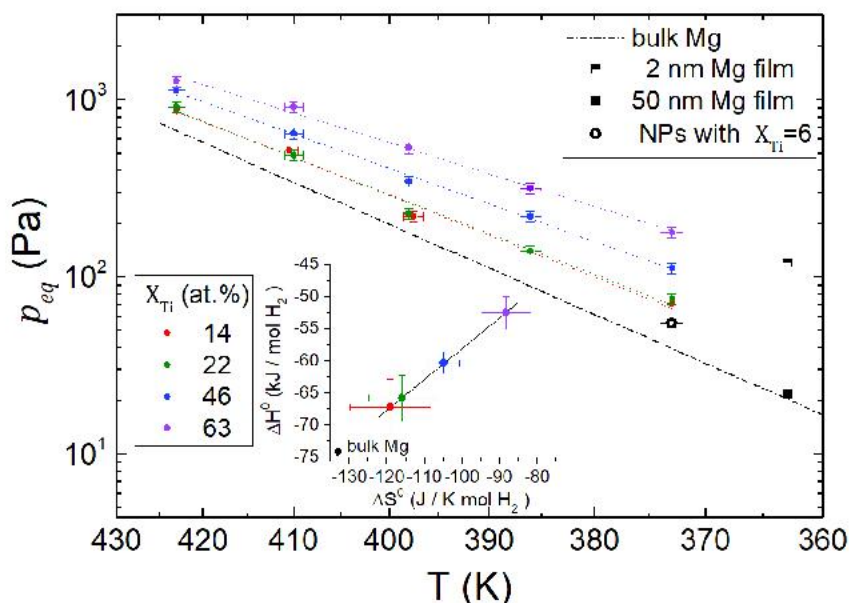


**Figure 5.** Collection of all  $p_{eq}$  vs  $T$  data for different  $X_{Ti}$  values as shown in the legend. The coloured dashed lines represent the best fits according to the van 't Hoff equation, from the slope and intercept of which we calculated the enthalpy and entropy data shown in the inset. The black dash-dotted line is a low-temperature extrapolation of bulk Mg data based on the values represented by the black circle in the inset ( $\Delta H_{bulk}^0 = -74.1$  kJ/molH<sub>2</sub> and  $\Delta S_{bulk}^0 = -133.4$  J/K · molH<sub>2</sub> [14]). For comparison, we also display the data measured at 90 °C on 2 and 50 nm thick Mg films embedded within TiH<sub>2</sub> layers [26], and at 100 °C on similar Mg-Ti-H NPs with  $X_{Ti} = 6$  at.% from a previous publication [33].

The enthalpy / entropy values obtained from the best fit parameters are displayed in the inset of **Figure 5** where the same colors used for  $p_{eq}$  data have been applied to distinguish samples with different Ti content. As one can see,  $\Delta H_{nano}^0$  and  $\Delta S_{nano}^0$  are affected by large uncertainties because the investigated temperature range, constrained by slow kinetics on the

low  $T$  side and by coarsening phenomena on the high  $T$  side, is too narrow to allow a robust determination of two fit parameters. Despite these uncertainties, it appears that both  $\Delta H_{nano}^0$  and  $\Delta S_{nano}^0$  depart from the bulk values represented by the black circle in the inset of **Figure 5** and that they exhibit a decreasing trend (in absolute value) with increasing  $X_{Ti}$ . The solid line in the inset of **Figure 5** is the best linear fit to the  $\Delta H_{nano}^0$  vs  $\Delta S_{nano}^0$  series. Its slope,  $T^* = 477 \pm 5$  K, represents an apparent enthalpy-entropy compensation temperature, i.e. a temperature, at which all samples have the same Gibbs free energy  $\Delta G_{nano}^0$  and therefore the same plateau pressure. The fact that  $T^*$  is well above the average temperature of the measurements may point to a genuine enthalpy-entropy compensation temperature. However, in our opinion a solid proof of such a compensation would require a more accurate determination of enthalpy and entropy through measurements over a more extended temperature range [40].

### 3.3 Hydrogen sorption kinetics

**Figure 6** displays the absorption kinetics measured at 150 °C on the same three samples of **Figure 4** for different hydrogen pressures  $p(H_2)$ , while **Figure 7** shows the corresponding desorption kinetics. As mentioned above, the kinetics were actually measured before the PCIs, carrying out 2 or 3 absorption/desorption cycles at each pressure with the aim to check reproducibility and stability. The sorption rate strongly depends on composition, the time necessary to attain 50% of the maximum  $H_2$  capacity clearly decreasing with increasing  $X_{Ti}$ . A collection of kinetics measured at 150 °C on all samples is provided in **Figure S5** of the Supporting Information. Inspection of kinetic data in **Figure S5a** reveals that the  $H_2$  absorption rate peaks at about 4.8 wt%/min for the two samples with  $X_{Ti} = 14$  and 22 at.%. The desorption rate is also quite good for these samples and increases further in sample Mg-35Ti-H as shown in **Figure S5b**. Moreover, the reversible gravimetric capacity peaks at about 4.8 wt%  $H_2$  for Mg-14Ti-H. Therefore, as far as reversible storage kinetics are concerned, the most appealing performances are found in the range  $X_{Ti} = 14 \div 35$  at.%. This result originates with two competing factors that intervene when the Ti content is increased, namely the speed up of the metal-hydride transformation and the loss of reversible capacity. There is no point in going to lower Ti contents because both the reversible capacity and the H-sorption rate appear to decrease.



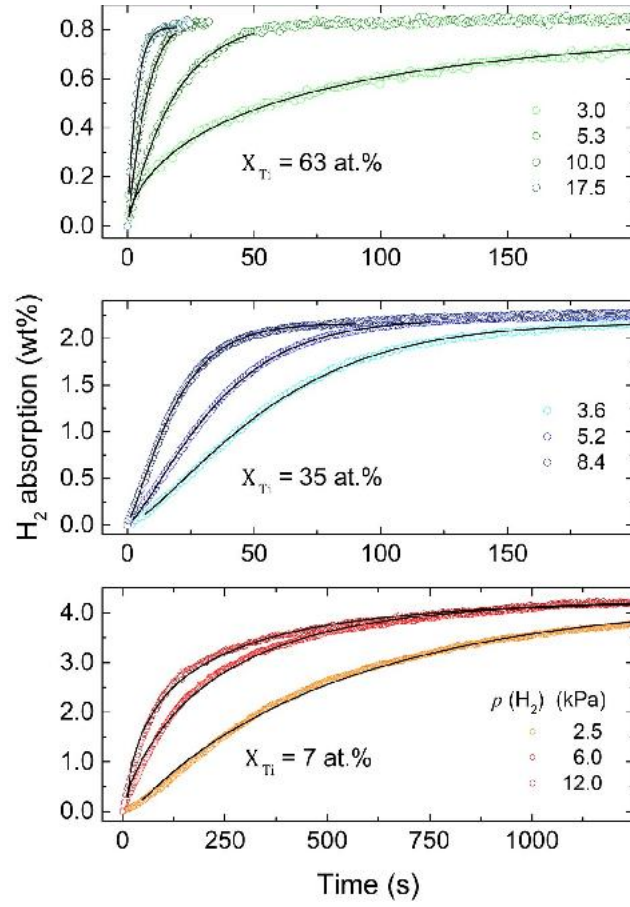


**Figure 6.** Hydrogen absorption kinetics recorded at 150 °C on the same samples of **Figure 4** with  $X_{Ti} = 7, 35$ , and 63 at.%. The data were acquired under quasi-isobaric conditions ( $\max \Delta p \approx 0.1$  kPa) at different starting pressures  $p(H_2)$  as indicated in the legend (increasing darkness of the symbol colors denotes increasing  $p(H_2)$ ). The black solid lines represent the best fits according to a nucleation and growth kinetics. Notice the different time scale used for  $X_{Ti} = 7$  at.% due to the significantly slower kinetics.

As concerns the pressure dependence of H-absorption, illustrated by symbols with different brightness in **Figure 6**, we clearly observe that the kinetics speed up with rising  $p(H_2)$ . The transformed fraction  $\alpha(t)$  is described well by the Johnson-Mehl-Avrami-Kolmogorov (JMAK) equation for nucleation and growth kinetics [34]:

$$\alpha(t) = 1 - \exp(-(k_{abs}t)^n) \quad (2)$$

The corresponding best-fit curves are displayed as solid lines in **Figure 5**. In all cases, the reaction order  $n$  is close to unity, a value compatible with instantaneous nucleation followed by 2-dimensional diffusion-controlled or 1-dimensional interface-controlled growth [34,41]. The rate constant  $k_{abs}$ , displayed in **Figure S6**, increases with  $X_{Ti}$  and appears to increase linearly with  $p(H_2)$ , as often reported for absorption kinetics [42]. The pressure dependence function  $f(p)$  of the kinetic rates has been discussed extensively by Ron [42], who reviewed different

forms of  $f(p)$  used in the literature. The most common forms for  $f(p)$  are compared in **Figure S7**, which confirms that the linear dependence is the one that best fits our  $k_{abs}$  values. This result can be explained considering that the flow of hydrogen from the environment toward the surface of the reacting material is proportional to  $p - p_{eq}$  [42]. The function  $f(p)$  must be inserted into the differential rate equation attributed to a specific mechanism or reaction order, i.e. nucleation and growth in the present case. For nearly isobaric kinetics with  $p$  well above  $p_{eq}$ , the integration is straightforward and yields the observed linear dependence of  $k_{abs}$  on the  $H_2$  pressure.

Our kinetic data show that the blocking layer effect is negligible in the biphasic NPs, even at low Ti content where after H-sorption cycles the average NPs diameter  $d_{NP}$  has grown to about 40 nm. In this context, it is worth to remark that Duan et al have also recently found fast in-plane H diffusion in thin Mg films deposited on a Ti-buffer layer [43]. In contrast to out-of-plane H diffusion there is absolutely no blocking effect for in-plane H diffusion. Therefore, we suggest that Mg/TiH<sub>2</sub> interfaces constitute accelerated paths for H diffusion also in our NPs. Using the mobility data of Duan et al it is possible to estimate that, if H-absorption were diffusion-limited, the loading time at 150 °C would be very short, i.e.  $\approx 0.01$  s for  $d_{NP} = 10$  nm and  $\approx 0.16$  s for  $d_{NP} = 40$  nm [43]. Since the H-absorption times visible in **Figure 6** are definitely much longer, we may deduce that the rate-limiting step of hydride growth is not given by in-plane H-diffusion. In conjunction with the above JMAK fitting, we therefore suggest that hydride forms by nucleation followed by 1-dimensional interface-controlled growth.

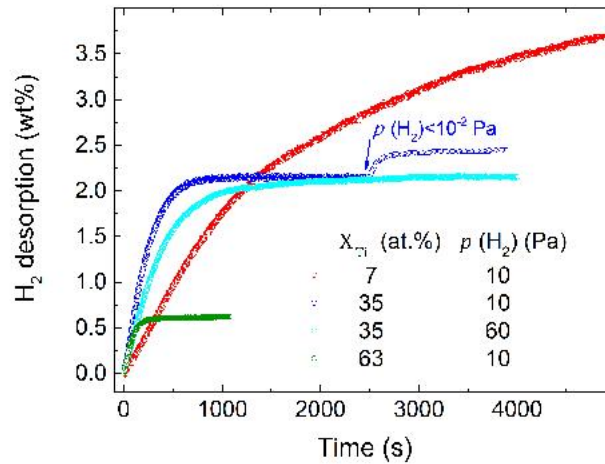


**Figure 7.** Hydrogen desorption kinetics recorded at 150 °C on the same samples of **Figure 4 and 5** with  $X_{Ti} = 7, 35$ , and 63 at.%. For  $X_{Ti} = 35$  at.%, measurements at two different initial pressures  $p(H_2)$  are reported. For this sample, we also show a final desorption step measured under high vacuum using the quadrupole mass spectrometer, that corresponds to the low-pressure plateau of **Figure 4**.

In the case of H-desorption kinetics, it was not possible to carry out measurements under nearly isobaric conditions due to the low desorption plateau pressure. In fact, the pressure rises significantly during hydrogen release from the sample, eventually approaching the plateau

pressure. Under these conditions, hydrogen release becomes so slow that it may be necessary to restore high vacuum in order to complete the desorption, as shown in **Figure 7** for Mg-35Ti-H. The dependence of the initial desorption rate on  $p(\text{H}_2)$ , already demonstrated in **Figure 7** for  $p(\text{H}_2) = 10$  and 60 Pa, is represented in **Figure S8** over a wider pressure range. A remarkably fast desorption rate of about 0.19 wt%/min is measured at  $p(\text{H}_2) = 100$  Pa.

### 3.4 Interface destabilization model for biphasic nanoparticles

The ratio  $p_{eq,nano}/p_{eq,bulk}$  can be converted into a free energy bias  $\delta\Delta G^0$ , i.e. a change of the reaction's free energy, through the simple equation [26,44]:

$$\delta\Delta G^0 \equiv \Delta G_{nano}^0 - \Delta G_{bulk}^0 = RT \ln \left( \frac{p_{eq,nano}}{p_{eq,bulk}} \right) \quad (3)$$

This thermodynamical bias is therefore the vertical distance from the bulk Mg line in **Figure 5** converted into suitable energy units. By inspection of **Figure 5**, one can easily realize that  $\delta\Delta G^0$  exhibits an increasing trend with increasing Ti content and that it decreases with increasing  $T$ .

In particular, at  $T = 100$  °C and  $X_{\text{Ti}} = 63$  at.%, we determined  $\delta\Delta G^0 \approx 4.7$  kJ/mol  $\text{H}_2$ , which corresponds to a pressure increase  $\frac{p_{eq,nano}}{p_{eq,bulk}} \approx 4.5$  and is very close to the bias measured in 2 nm thick Mg films sandwiched within  $\text{TiH}_2$  [26]. By comparison, the standard free energy for bulk  $\text{MgH}_2$  formation at  $T = 100$  °C is  $\Delta G_{bulk}^0 = \Delta H_{bulk}^0 - 373 \cdot \Delta S_{bulk}^0 = -24.3$  kJ/mol  $\text{H}_2$ . These results are relevant because they show an altered thermodynamics of hydrogen in Mg-based NPs from both absorption and desorption experiments, while previous reports were based solely on absorption data [45,46].

Three main causes may be responsible *a priori* for the observed thermodynamical bias. The first is the presence of Ti atoms in solid solution within the Mg/ $\text{MgH}_2$  lattice. However, this can be excluded because the lattice parameter should change with Ti content, in contradiction with the results of XRD analysis. The second is the strain associated with elastic constraints in a multiphase nanostructured material [24,47]. While this effect can dominate the behavior of thin films rigidly attached on a substrate and of fully encapsulated nano-objects, we suggest that it plays a minor role here, since the NPs are free to expand outward and because the Mg/ $\text{TiH}_2$  interface provides only a very weak clamping [48]. The third is the change of the interface free energy upon hydride formation and decomposition, that can induce a thermodynamical bias according to [23–26]:

$$\delta\Delta G^0 = \int_{hyd} \gamma_{hyd} \cdot dA - \int_{met} \gamma_{met} \cdot dA \quad (4)$$

Where  $\gamma_{hyd}$  ( $\gamma_{met}$ ) is the interface free energy per unit area in the hydride (metal) phase. The integrals are calculated over all interfaces in either the hydride or metal phase and are normalized to one mole of Mg. There are some relatively simple cases, in which the total interface area  $A_{int}$  per mole of Mg does not change upon hydride formation/decomposition. If this is so, the bias becomes simply  $\delta\Delta G^0 = A_{int} \cdot \Delta\gamma$  where  $\Delta\gamma \equiv \gamma_{hyd} - \gamma_{met}$ . Clearly,  $A_{int}$

depends on sample microstructure and/or composition. One example is provided by Mg/MgH<sub>2</sub> thin films of thickness  $d$  embedded within TiH<sub>2</sub> layers, for which Mooij et al have shown that [26]:

$$\delta\Delta G^0 = A_{int} \cdot \Delta\gamma = \frac{2\bar{V}_{Mg}}{d} \Delta\gamma \quad (5)$$

where  $\bar{V}_{Mg} = 13.98 \cdot 10^{-6} \text{ m}^3$  is the molar volume of Mg. Another case, relevant for the modelling of our samples in the limit of low Ti content, is that of separated TiH<sub>2</sub> nano-crystallites of diameter  $d_{TiH_2}$  embedded within larger Mg/MgH<sub>2</sub> NPs. **Figure 8** illustrates the essential features of hydride formation in such a nanostructure highlighting the interface regions. In this case  $\Delta\gamma$  represents an average over the different crystallographic orientations of the involved interfaces. As detailed in the Supporting Information, the thermodynamical bias is inversely proportional to  $d_{TiH_2}$  and augments with increasing Ti content according to:

$$\delta\Delta G^0 = A_{int} \cdot \Delta\gamma = \frac{6\bar{V}_{TiH_2}}{d_{TiH_2}} \frac{X_{Ti}}{100-X_{Ti}} \cdot \Delta\gamma \quad (6)$$

where  $\bar{V}_{TiH_2} = 13.30 \cdot 10^{-6} \text{ m}^3$  is the molar volume of TiH<sub>2</sub>.

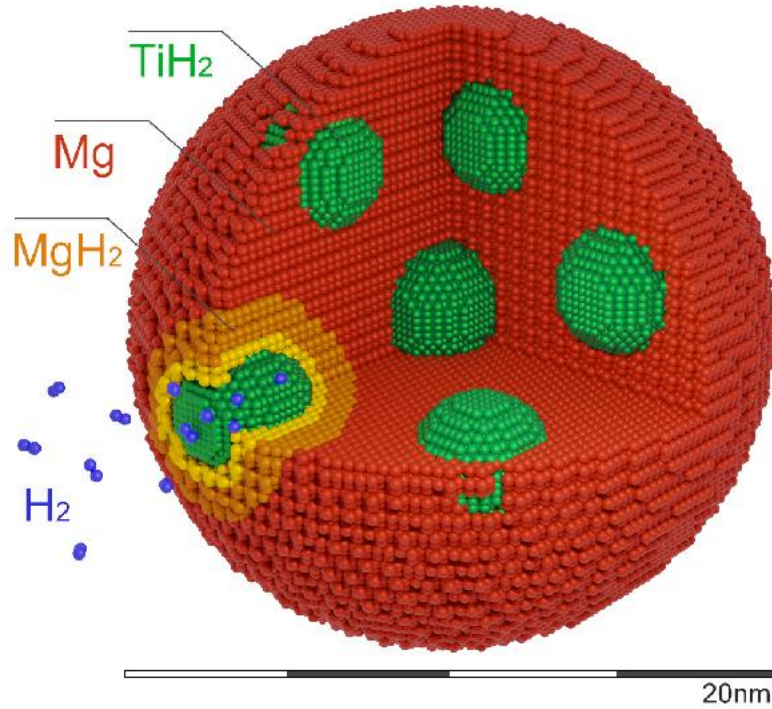


**Figure 8.** Schematic 3-dimensional section of one Mg-Ti-H biphasic nanoparticle for low Ti content. The H<sub>2</sub> molecules dissociate at the surface of an ultra-small TiH<sub>2</sub> crystallite. Nucleation and growth of MgH<sub>2</sub>, represented in orange, is expected to take place more easily around TiH<sub>2</sub>. The MgH<sub>2</sub>/ TiH<sub>2</sub> interface region is visualized in yellow.

The interface area considered is the one between Mg (or MgH<sub>2</sub>) and TiH<sub>2</sub>, schematically visualized in yellow in **Figure 8**. These models take into account neither homophasic interfaces, such as grain boundaries, nor the outer surfaces of the NPs. These may contribute to an additional bias but our assumption seems justified given the observed dependence on the Ti content. One can therefore convert  $X_{\text{Ti}}$  into  $A_{\text{int}}$  by means of the microstructure parameters reported in Table S1, considering also the contact between TiH<sub>2</sub> crystallites at high  $X_{\text{Ti}}$  [49], as discussed in the Supporting Information. The interfacial free energy difference  $\Delta\gamma$  is then simply obtained by a linear fit of  $\delta\Delta G^0$  versus  $A_{\text{int}}$ . This procedure is illustrated in **Figure 9** for the two extreme temperatures. We obtain  $\Delta\gamma = (0.20 \pm 0.02) \text{ J m}^{-2}$  at  $T = 150^\circ\text{C}$  and  $\Delta\gamma = (0.38 \pm 0.04)$  at  $T = 100^\circ\text{C}$ . These values should be compared with those obtained in MgH<sub>2</sub> thin films using Equation (5), for which the authors reported  $\Delta\gamma \approx 0.22 \text{ J m}^{-2}$  at  $150^\circ\text{C}$  and  $\Delta\gamma \approx 0.33 \text{ J m}^{-2}$  at  $90^\circ\text{C}$  [26]. The good agreement supports our interpretation that the observed thermodynamical bias in MgH<sub>2</sub>-TiH<sub>2</sub> biphasic NPs originates with interface free energy difference between hydride and metal phase.

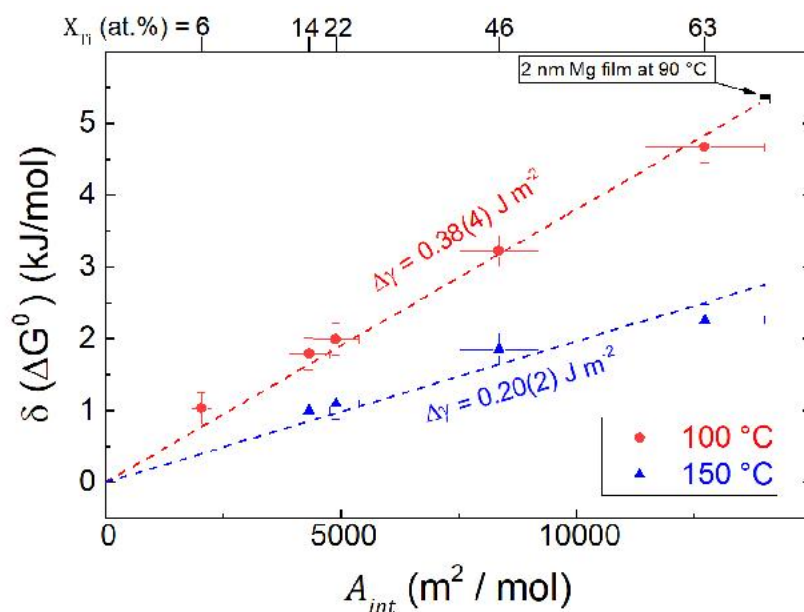


**Figure 9.** Thermodynamical bias  $\delta\Delta G^0$ , calculated from the data in **Figure 7** at  $T = 100$  and  $150^\circ\text{C}$  using Equation (3), as a function of the interface area  $A_{\text{int}}$  obtained from  $X_{\text{Ti}}$  by means of microstructural parameters (see Supporting Information for further details). The original  $X_{\text{Ti}}$  values are marked on the top horizontal axis. The dashed lines represent the best linear fits, from which the interfacial free energy difference  $\Delta\gamma$  is determined. The point measured by Mooij et al on 2 nm Mg thin films [26] is marked by an arrow. The point for  $X_{\text{Ti}} = 6$  at.% on the data set at  $T = 100^\circ\text{C}$  is taken from a previous publication on similar Mg-Ti-H NPs [33].

## 4. Conclusions

In this work, we have proposed the new concept of biphasic nanoparticles for hydrogen storage, in which two bulk-immiscible phases are intimately mixed within single nanoparticles:  $\text{TiH}_2$  provides catalytic activity for  $\text{H}_2$  dissociation and recombination as well as paths for accelerated diffusion of atomic hydrogen, whereas  $\text{MgH}_2$  conveys reversible H-storage capacity under mild pressure/temperature conditions. Differently from previous reports on Mg thin films, we do not make use of Pd catalyst and the morphology is compatible with scale-up. The peculiar nanostructure permits to achieve full absorption (desorption) within tens of seconds (minutes) at the remarkably low temperature of 150 °C, where hydrogen desorption kinetics have never been reported in conventional ball-milled Mg-based nanostructured powders.

Moreover, equilibrium data collected in the 100 – 150 °C range reveal a composition-dependent thermodynamics of hydrogen sorption. The thermodynamical bias  $\delta\Delta G^0$ , a measure of the free energy difference compared to bulk Mg, tends to increase with increasing Ti content  $X_{\text{Ti}}$ , indicating destabilization of the hydride. In particular, we measure  $\delta\Delta G^0 \approx 4.7 \text{ kJ/mol H}_2$  at  $T = 100 \text{ °C}$  and  $X_{\text{Ti}} = 63 \text{ at.}\%$ , which corresponds to an increase of the pressure for hydride formation/decomposition by a factor of  $\approx 4.5$ . This means that, with increasing Ti content, the conditions for hydrogen desorption become more favorable than for bulk Mg. However, this thermodynamic alteration comes at the cost of a reduced gravimetric capacity linked with the high weight fraction of  $\text{TiH}_2$ .

We show that a model based on interface - induced destabilization explains well the observed hydrogen sorption thermodynamics. Accordingly, by analyzing the dependence of  $\delta\Delta G^0$  on composition and microstructure we obtained an interfacial free energy difference  $\Delta\gamma = 0.40(4)$  and  $0.20(2) \text{ Jm}^{-2}$  at  $T = 100$  and  $150 \text{ °C}$ , respectively, in excellent agreement with the  $\Delta\gamma$  values reported for model 2-dimensional films [26]. The van 't Hoff analysis and the temperature dependence of  $\delta\Delta G^0$  suggest that  $\Delta\gamma$  contains an enthalpic and an entropic contribution, the latter partly compensating the destabilization induced by the former. Therefore, further advances in destabilization of  $\text{MgH}_2$  nanostructures would certainly benefit from a progress in the modelling and engineering of the interfacial entropy.

In summary, this work proves that properly designed nanostructures can significantly stretch the temperature / pressure window for fast Mg-based hydrogen sorption toward ambient conditions.

## Acknowledgements

Financial support from the Italian Ministry of University and Research (MIUR) within PRIN-2015 Project NEWLI is gratefully acknowledged.

## References

- [1] S. Park, Y. Shao, J. Liu, Y. Wang, Oxygen electrocatalysts for water electrolyzers and reversible fuel cells: Status and perspective, *Energy Environ. Sci.* 5 (2012) 9331–9344.



doi:10.1039/c2ee22554a.

- [2] R. van de Krol, M. Grätzel, Photoelectrochemical hydrogen production, Springer, Boston, MA, 2012. doi:<https://doi.org/10.1007/978-1-4614-1380-6>.
- [3] L. Carrette, K.A. Friedrich, U. Stimming, Fuel Cells - Fundamentals and Applications, Fuel Cells. 1 (2001) 5–39. doi:10.1002/1615-6854(200105)1:1<5::aid-fuce5>3.0.co;2-g.
- [4] B.C.H. Steele, A. Heinzel, Materials for fuel-cell technologies, Nature. 414 (2001) 345–352. doi:10.1038/35104620.
- [5] A. Züttel, Materials for hydrogen storage, Mater. Today. (2003) 24–33.
- [6] E. Callini, K.-F. Aguey-Zinsou, R. Ahuja, J.R. Ares, S. Bals, N. Biliškov, S. Chakraborty, G. Charalambopoulou, A.-L. Chaudhary, F. Cuevas, B. Dam, P. de Jongh, M. Dornheim, Y. Filinchuk, J. Grbović Novaković, M. Hirscher, T.R. Jensen, P.B. Jensen, N. Novaković, Q. Lai, F. Leardini, D.M. Gattia, L. Pasquini, T. Steriotis, S. Turner, T. Vegge, A. Züttel, A. Montone, Nanostructured materials for solid-state hydrogen storage: A review of the achievement of COST Action MP1103, Int. J. Hydrogen Energy. 41 (2016) 14404–14428. doi:10.1016/j.ijhydene.2016.04.025.
- [7] V.A. Yartys, M.V. Lototsky, E. Akiba, R. Albert, V.E. Antonov, J.R. Ares, M. Baricco, N. Bourgeois, C.E. Buckley, J.M. Bellosta von Colbe, J.-C. Crivello, F. Cuevas, R.V. Denys, M. Dornheim, M. Felderhoff, D.M. Grant, B.C. Hauback, T.D. Humphries, I. Jacob, T.R. Jensen, P.E. de Jongh, J.-M. Joubert, M.A. Kuzovnikov, M. Latroche, M. Paskevicius, L. Pasquini, L. Popilevsky, V.M. Skripnyuk, E. Rabkin, M.V. Sofianos, A. Stuart, G. Walker, H. Wang, C.J. Webb, M. Zhu, Magnesium based materials for hydrogen based energy storage: Past, present and future, Int. J. Hydrogen Energy. 44 (2019) 7809–7859. doi:10.1016/j.ijhydene.2018.12.212.
- [8] J.-C. Crivello, B. Dam, R. V. Denys, M. Dornheim, D.M. Grant, J. Huot, T.R. Jensen, P. de Jongh, M. Latroche, C. Milanese, D. Milčius, G.S. Walker, C.J. Webb, C. Zlotea, V.A. Yartys, Review of magnesium hydride-based materials: development and optimisation, Appl. Phys. A. 122 (2016) 97. doi:10.1007/s00339-016-9602-0.
- [9] C. Zlotea, Y. Oumellal, S.-J. Hwang, C.M. Ghimbeu, P.E. de Jongh, M. Latroche, Ultrasmall MgH<sub>2</sub> Nanoparticles Embedded in an Ordered Microporous Carbon Exhibiting Rapid Hydrogen Sorption Kinetics, J. Phys. Chem. C. 119 (2015) 18091–18098. doi:10.1021/acs.jpcc.5b05754.
- [10] P.E. De Jongh, P. Adelhelm, Nanosizing and nanoconfinement: New strategies towards meeting hydrogen storage goals, ChemSusChem. 3 (2010) 1332–1348. doi:10.1002/cssc.201000248.
- [11] T. Vegge, Locating the rate-limiting step for the interaction of hydrogen with Mg(0001) using Density-Functional Theory calculations and rate theory, Phys. Rev. B - Condens. Matter Mater. Phys. 70 (2004) 1–7. doi:10.1103/PhysRevB.70.035412.
- [12] S. Kumar, T. Pavludis, V. Singh, H. Nguyen, S. Steinhauer, C. Pursell, B. Clemens, J.



- Kioseoglou, P. Grammatikopoulos, M. Sowwan, Hydrogen Flux through Size Selected Pd Nanoparticles into Underlying Mg Nanofilms, *Adv. Energy Mater.* 8 (2018) 1701326. doi:10.1002/aenm.201701326.
- [13] H.T. Uchida, R. Kirchheim, A. Pundt, Influence of hydrogen loading conditions on the blocking effect of nanocrystalline Mg films, *Scr. Mater.* 64 (2011) 935–937. doi:10.1016/j.scriptamat.2011.01.036.
- [14] M. Paskevicius, D.A. Sheppard, C.E. Buckley, Thermodynamic Changes in Mechanochemically Synthesized Magnesium Hydride Nanoparticles, *J. Am. Chem. Soc.* 6 (2010) 469–472. doi:10.1021/ja908398u.
- [15] Y. Fukai, *The Metal-Hydrogen System: Basic Bulk Properties*, Springer-Verlag, Berlin-Heidelberg, 2005.  
<https://books.google.it/books?hl=it&lr=&id=CshrlxMIQaoC&oi=fnd&pg=PA1&dq=fukai+the+metal+hydrogen&ots=Xa8BRZprxG&sig=Xj4-Wjo4imdV9l2uKWHQ0WhXsug#v=onepage&q=fukai+the+metal+hydrogen&f=false>  
 (accessed December 6, 2019).
- [16] J. Harris, On the adsorption and desorption of H<sub>2</sub> at metal surfaces, *Appl. Phys. A Solids Surfaces.* 47 (1988) 63–71. doi:10.1007/BF00619699.
- [17] F. Cuevas, D. Korablov, M. Latroche, Synthesis, structural and hydrogenation properties of Mg-rich MgH<sub>2</sub>–TiH<sub>2</sub> nanocomposites prepared by reactive ball milling under hydrogen gas, *Phys. Chem. Chem. Phys.* 14 (2012) 1200. doi:10.1039/c1cp23030a.
- [18] A. Zaluska, L. Zaluski, J.O. Ström-Olsen, Structure, catalysis and atomic reactions on the nano-scale: a systematic approach to metal hydrides for hydrogen storage, *Appl. Phys. A Mater. Sci. Process.* 72 (2001) 157–165. doi:10.1007/s003390100783.
- [19] G. Barkhordarian, T. Klassen, R. Bormann, Catalytic mechanism of transition-metal compounds on Mg hydrogen sorption reaction, *J. Phys. Chem. B.* 110 (2006) 11020–11024. doi:10.1021/jp0541563.
- [20] P. Rizo-Acosta, F. Cuevas, M. Latroche, Hydrides of early transition metals as catalysts and grain growth inhibitors for enhanced reversible hydrogen storage in nanostructured magnesium, *J. Mater. Chem. A.* 7 (2019) 23064. doi:10.1039/c9ta05440e.
- [21] Y.J. Choi, J. Lu, H.Y. Sohn, Z.Z. Fang, E. Rönnebro, Effect of Milling Parameters on the Dehydrogenation Properties of the Mg-Ti-H System, *J. Phys. Chem. C.* 113 (2009) 19344–19350. doi:10.1021/jp907218t.
- [22] G. Barkhordarian, T. Klassen, R. Bormann, Fast hydrogen sorption kinetics of nanocrystalline Mg using Nb<sub>2</sub>O<sub>5</sub> as catalyst, *Scr. Mater.* 49 (2003) 213–217. doi:10.1016/S1359-6462(03)00259-8.
- [23] K.C. Kim, B. Dai, J. Karl Johnson, D.S. Sholl, Assessing nanoparticle size effects on metal hydride thermodynamics using the Wulff construction., *Nanotechnology.* 20 (2009) 204001. doi:10.1088/0957-4484/20/20/204001.

- [24] L. Pasquini, The Effects of Nanostructure on the Hydrogen Sorption Properties of Magnesium-Based Metallic Compounds: A Review, *Crystals*. 8 (2018) 106. doi:10.3390/cryst8020106.
- [25] V. Bérubé, G. Radtke, M. Dresselhaus, G. Chen, Size effects on the hydrogen storage properties of nanostructured metal hydrides: A review, *Int. J. Energy Res.* 31 (2007) 637–663. doi:10.1002/er.1284.
- [26] L.P.A. Mooij, A. Baldi, C. Boelsma, K. Shen, M. Wagemaker, Y. Pivak, H. Schreuders, R. Griessen, B. Dam, Interface energy controlled thermodynamics of nanoscale metal hydrides, *Adv. Energy Mater.* 1 (2011) 754–758. doi:10.1002/aenm.201100316.
- [27] K. Asano, R.J. Westerwaal, A. Anastasopol, L.P.A. Mooij, C. Boelsma, P. Ngene, H. Schreuders, S.W.H. Eijt, B. Dam, Destabilization of Mg Hydride by Self-Organized Nanoclusters in the Immiscible Mg-Ti System, *J. Phys. Chem. C*. 119 (2015) 12157–12164. doi:10.1021/acs.jpcc.5b02275.
- [28] K. Yoshimura, C. Langhammer, B. Dam, Metal hydrides for smart window and sensor applications, *MRS Bull.* . 38 (2013) 495-503. doi:10.1557/mrs.2013.129.
- [29] C. Gammer, C. Mangler, C. Rentenberger, H.P. Karnthaler, Quantitative local profile analysis of nanomaterials by electron diffraction, *Scr. Mater.* 63 (2010) 312–315. doi:10.1016/J.SCRIPMAT.2010.04.019.
- [30] G. Ischia, H.-R. Wenk, L. Lutterotti, F. Berberich, Quantitative Rietveld texture analysis of zirconium from single synchrotron diffraction images, *J. Appl. Crystallogr.* 38 (2005) 377–380. doi:10.1107/S0021889805006059.
- [31] C.G. Granqvist, R.A. Buhrman, Ultrafine metal particles, *J. Appl. Phys.* 47 (1976) 2200–2219. doi:10.1063/1.326081.
- [32] M.L. Eggersdorfer, S.E. Pratsinis, Agglomerates and aggregates of nanoparticles made in the gas phase, *Adv. Powder Technol.* 25 (2014) 71–90. doi:10.1016/j.appt.2013.10.010.
- [33] N. Patelli, M. Calizzi, A. Migliori, V. Morandi, L. Pasquini, Hydrogen Desorption Below 150 °C in MgH<sub>2</sub>–TiH<sub>2</sub> Composite Nanoparticles: Equilibrium and Kinetic Properties, *J. Phys. Chem. C*. 121 (2017) 11166–11177. doi:10.1021/acs.jpcc.7b03169.
- [34] N. Patelli, A. Migliori, L. Pasquini, Reversible Metal-Hydride Transformation in Mg-Ti-H Nanoparticles at Remarkably Low Temperatures, *ChemPhysChem*. 20 (2019) 1325–1333. doi:10.1002/cphc.201801186.
- [35] M. Calizzi, F. Venturi, M. Ponthieu, F. Cuevas, V. Morandi, T. Perkisas, S. Bals, L. Pasquini, Gas-phase synthesis of Mg–Ti nanoparticles for solid-state hydrogen storage, *Phys. Chem. Chem. Phys.* 18 (2016) 141–148. doi:10.1039/C5CP03092G.
- [36] A. Surrey, K. Nielsch, B. Rellinghaus, Comments on “Evidence of the hydrogen release mechanism in bulk MgH<sub>2</sub>”, *Sci. Rep.* 7 (2017) 44216. doi:10.1038/srep44216.

- [37] R. Gremaud, A. Baldi, M. Gonzalez-Silveira, B. Dam, R. Griessen, Chemical short-range order and lattice deformations in Mg<sub>1-y</sub>Ti<sub>1-y</sub>H<sub>x</sub> thin films probed by hydrogenography, *Phys. Rev. B - Condens. Matter Mater. Phys.* 77 (2008) 1–10. doi:10.1103/PhysRevB.77.144204.
- [38] A. Baldi, L. Mooij, V. Palmisano, H. Schreuders, G. Krishnan, B.J. Kooi, B. Dam, R. Griessen, Elastic versus Alloying Effects in Mg-Based Hydride Films, *Phys. Rev. Lett.* 121 (2018) 255503. doi:10.1103/PhysRevLett.121.255503.
- [39] A. Molinari, F. D’Amico, M. Calizzi, Y. Zheng, C. Boelsma, L. Mooij, Y. Lei, H. Hahn, B. Dam, L. Pasquini, Interface and strain effects on the H-sorption thermodynamics of size-selected Mg nanodots, *Int. J. Hydrogen Energy*. 41 (2016) 9841–9851. doi:10.1016/j.ijhydene.2016.02.003.
- [40] A. Cornish-Bowden, Enthalpy-entropy compensation: a phantom phenomenon., *J. Biosci.* 27 (2002) 121–126. doi:10.1007/BF02703768.
- [41] L. Pasquini, E. Callini, E. Piscopiello, A. Montone, M.V. Antisari, E. Bonetti, Metal-hydride transformation kinetics in Mg nanoparticles, *Appl. Phys. Lett.* 94 (2009) 041918. doi:10.1063/1.3077186.
- [42] M. Ron, The normalized pressure dependence method for the evaluation of kinetic rates of metal hydride formation/decomposition, *J. Alloys Compd.* 283 (1999) 178–191. doi:10.1016/S0925-8388(98)00859-7.
- [43] X. Duan, R. Griessen, R.J. Wijngaarden, S. Kamin, N. Liu, Self-recording and manipulation of fast long-range hydrogen diffusion in quasifree magnesium, *Phys. Rev. Mater.* 2 (2018) 085802. doi:10.1103/PhysRevMaterials.2.085802.
- [44] L. Pasquini, The effects of nanostructure on the hydrogen sorption properties of magnesium-based metallic compounds: A review, *Crystals*. 8 (2018). doi:10.3390/cryst8020106.
- [45] Z. Zhao-Karger, J. Hu, A. Roth, D. Wang, C. Kübel, W. Lohstroh, M. Fichtner, Altered thermodynamic and kinetic properties of MgH<sub>2</sub> infiltrated in microporous scaffold., *Chem. Commun. (Camb)*. 46 (2010) 8353–5. doi:10.1039/c0cc03072d.
- [46] A. Anastasopol, T. V. Pfeiffer, J. Middelkoop, U. Lafont, R.J. Canales-Perez, A. Schmidt-Ott, F.M. Mulder, S.W.H. Eijt, Reduced enthalpy of metal hydride formation for Mg-Ti nanocomposites produced by spark discharge generation, *J. Am. Chem. Soc.* 135 (2013) 7891–7900. doi:10.1021/ja3123416.
- [47] A. Baldi, M. Gonzalez-Silveira, V. Palmisano, B. Dam, R. Griessen, Destabilization of the Mg-H system through elastic constraints, *Phys. Rev. Lett.* 102 (2009) 1–4. doi:10.1103/PhysRevLett.102.226102.
- [48] A. Baldi, V. Palmisano, M. Gonzalez-Silveira, Y. Pivak, M. Slaman, H. Schreuders, B. Dam, R. Griessen, Quasifree Mg-H thin films, *Appl. Phys. Lett.* 95 (2009) 20–22. doi:10.1063/1.3210791.

- [49] A.M. Brasil, T.L. Farias, M.G. Carvalho, A recipe for image characterization of fractal-like aggregates, *J. Aerosol Sci.* 30 (1999) 1379–1389. doi:10.1016/S0021-8502(99)00026-9.

## Vitae



**Nicola Patelli** received his MSc Degree in Physics in 2016 from the University of Bologna and he is on the way to defend the Ph.D. title in 2020. During the doctoral research, he worked on the growth and characterization of nanoparticles and nanocomposites for energy applications at the University of Bologna and at the Institute of Nanotechnology of the Karlsruhe Institute of Technology. Currently, his research interests focus on the development of nanostructures with controlled morphology, composition and chemistry via gas phase condensation experiments integrated with modeling and computer simulation.



**Andrea Migliori**, Ph.D. is Researcher at CNR-IMM Institute, Bologna Italy. The main part of his activity has been involved in microstructural and micro-analytical characterization of High  $T_c$  superconductor, semiconductors and related materials by means of Transmission Electron Microscopy techniques. The main current research topics deal with the structure determination of new materials using electron crystallographic methods and the microstructural and microanalytical characterization of nano-structured materials. He is author of more than 150 publications on international journals and proceedings of international conferences.



**Vittorio Morandi**, Ph.D. (ORCID: <https://orcid.org/0000-0002-8533-1540>) is Senior Researcher and Deputy Director of the Unit of Bologna of the CNR-IMM Institute (<http://www.bo.imm.cnr.it>), chair and member of committees of several international conferences, and permanent reviewer of international projects and top-level scientific journals. He is directly involved in several national and international research projects and industrial contracts, and has published more than 130 papers (H=30) on international peer-reviewed journals. His main research interests concern the development of advanced electron microscopy techniques, their application to the study of nanomaterials, and the synthesis, characterization, and technological integration of graphene and graphene-based materials.



**Luca Pasquini** received the Ph.D. in Condensed Matter Physics at the University of Bologna. He worked as post-doc at the University of Stuttgart, the ESRF synchrotron and the University of Bologna, where he is currently Associate Professor of experimental materials physics. He has over 20 years of experience on the growth of nanoparticles and nanostructures by physical methods and on the investigation of structure-property relationships. He is author of about 110 papers on international journals (ORCID: <https://orcid.org/0000-0001-8939-2204>). His current research interests include hydride materials for solid-state hydrogen storage and semiconducting oxide nanostructures for solar energy conversion.